Gap-Plasmon-Enhanced Nanofocusing Near-Field Microscopy

Simon F. Becker,[*,†] Martin Esmann,[†] KyungWan Yoo,[†,‡] Petra Gross,[†] Ralf Vogelgesang,[†] NamKyoo Park,[‡] and Christoph Lienau[†]

[†]Institut für Physik and Center of Interface Science, Carl von Ossietzky Universität, D-26111 Oldenburg, Germany
[‡]Photonic Systems Laboratory, School of EECS, Seoul National University, Seoul 151-744, South Korea

S Supporting Information

ABSTRACT: We report the observation of coherent light scattering from nanometer-sized gap regions in a nanofocusing scanning near-field optical microscope. When approaching a nanofocusing gold taper to the surface of a thin semitransparent gold film and detecting in transmission, we find a steep increase in scattering intensity over the last 5 nm in a near-field signal selected in k-space. This is confirmed as a signature of highly confined gap plasmons by detailed comparisons to finite element method simulations. The simulations reveal that the confinement is adjustable via the underlying probe—sample distance control scheme even to levels well below the taper apex radius. This controlled experimental realization of gap plasmons and the extraction of their signature in a scanning probe microscope pave the way toward broadband spectroscopy at and below single-nanometer length scales, using parallel detection at multiple wavelengths, for instance, in transient absorption or two-dimensional spectroscopy.

KEYWORDS: nanofocusing, near-field microscopy, gap plasmon, nanospectroscopy
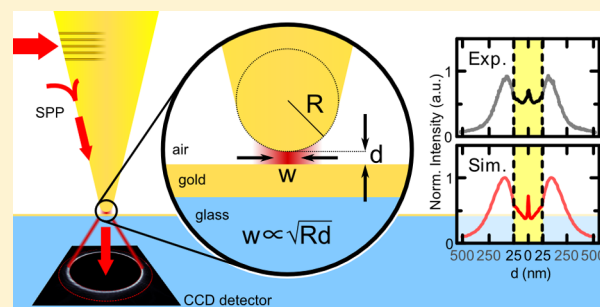
Nanospectroscopy, specifically nanoimaging at the single quantum emitter level augmented with broadband spectroscopic resolution, has been a longstanding goal[1−4] of nano-optics. Ultimately, it may also be combined with pump—probe measurement schemes,[5,6] such as transient absorption or two-dimensional spectroscopy, in order to investigate ultrafast optical transitions such as the primary processes of light harvesting[7,8] and photocatalytic reactions at nanostructured surfaces.[9,10] Dense and heterogeneous systems remain a particular challenge to extinction nanospectroscopy of single entities that aims at simultaneous (multichannel) detection at multiple wavelengths. First, selectively addressing nanoscopic volumes and probing their optical transitions in a natural environment requires reducing excitation of the neighborhood, which would result in parasitic background signals. Second, a better match of the cross-sectional area of the optical excitation fields and the interaction cross-sections of the optical transitions involved increases the probability per incident photon to excite the quantum emitter, which is given as the ratio of interaction cross-section and cross-sectional area of the excitation light source.

In this context, a suitable scheme is called for, which is capable of spatially confining optical excitation fields to single-nanometer-sized volumes and below. Here, the concept of adiabatic nanofocusing[11−14]—applied to apertureless scanning near-field optical microscopy (SNOM)—provides a promising approach. In essence, nanofocusing refers to spatial confinement of a surface plasmon polariton (SPP) field propagating along a tapered waveguide. This SPP field may be launched, for example, by coupling far field light to a grating coupler. As such, nanofocusing introduces a spatial separation of far-field excitation and a nanoconfined light source beneath the apex of a conical plasmonic taper. In addition, it has also been shown that the temporal structure of ultrashort excitation pulses emitted from the apex is almost unaffected by the nanofocusing process,[15,16] which will benefit the implementation of ultrafast pump—probe schemes.

Experimentally, a spatial resolution of ∼10 nm has been demonstrated in nanofocusing SNOM,[15,17] which is set, as in other apertureless SNOM schemes,[18−21] by the radius of curvature at the apex. In recent years, this radius appears to have leveled off at 5−10 nm due to nanofabrication limitations. Adiabatic nanofocusing with such tapers has been shown to yield convincing results for the investigation of plasmonic and other nanoparticles[15,22,23] and in principle allows exciting and detecting them individually. However, even smaller apex radii are required for routine investigations of *single quantum emitters*, which are notoriously difficult to observe by diffraction-limited optics, due to the large focal areas on the order of 10^{-8} cm^2. In comparison, for electronic transitions in molecular systems the absorption cross-sections are on the order of 10^{-16} to 10^{-14} cm^2.[24] Hence the accompanying signal levels are usually too small to be discriminated against background in far-field multichannel spectroscopy. To alleviate these experimental

challenges, easily controllable nanometer-sized light−matter interaction volumes are highly desirable.

One possible way to further push the confinement of electromagnetic near-fields in this direction is so-called gap plasmons, which form in the narrow opening between metallic structures. They have been studied in a variety of metal−insulator−metal configurations such as opposing nanowires and nanowires on surfaces,[25] opposing spheres,[26] spheres on surfaces,[27−29] and also conical tips over flat surfaces with far-field illumination.[30,31] An estimate for the lateral confinement of the gap plasmon was developed for tunnel junctions between taper probes and flat surfaces.[32] According to this well-established rule, the lateral confinement $w \propto \sqrt{Rd}$ is proportional to the square root of both the probe's apex radius of curvature R and the gap separation d. The ultimate lower boundary on w is reached for $d \approx 0.3$ nm due to the onset of quantum tunneling.[26]

In this work, we address the possibility of utilizing gap plasmons for improving the lateral near-field confinement with nanofocusing SNOM tapers. We approach a semitransparent $h = 30$ nm thick gold film to such a taper and detect elastically scattered radiation in transmission geometry. Angle-resolved (k-space) images reveal a clear signature of radiation originating from the gap formed between the taper and the sample: For angles beyond the critical angle of total internal reflection, we identify the formation of gap plasmons by rapid intensity changes for tip−sample distances of less than 10 nm. We confirm this connection via detailed comparison to finite element method (FEM) simulations, which facilitate a quantitative discussion of the transition from an apex mode to an adjustable, few-nanometer-sized gap plasmon.

■ RESULTS

In the following, we study the coupling between nanofocused near-fields at the apex of a conical gold taper and SPP modes of a gold-coated glass substrate. Specifically, we investigate the distance dependence of resonant light scattering from the apex for tip−sample distances down to single nanometers. Tapers with opening angles of $25° \pm 5°$, apex radii around 10 nm, and smooth surfaces were produced from single-crystalline gold wires by electrochemical etching (see Methods).[15] A grating coupler optimized for a laser wavelength of 800 nm was milled into one side of the taper shaft by focused ion beam lithography (Figure 1a), at a distance of ∼30 μm from the apex. As shown schematically in Figure 1c, the grating is illuminated with near-infrared laser light from a pulsed Ti:sapphire oscillator operating at $\lambda_0 = 800$ nm center wavelength. Since the taper is rotationally symmetric, the supported SPP modes are characterized by their angular momentum number m and azimuthal field dependence $\exp(im\phi)$. Grating coupling launches a superposition of those eigenmodes. As Figure 1b shows, the SPPs propagate along the smooth taper surface without much scattering. Higher order modes ($m \neq 0$) are surface-bound modes only for sufficiently large radii.[34] On their way toward the apex they get converted into unbound far-field radiation at specific critical radii. In contrast, the $m = 0$ mode remains bound to the taper and gets adiabatically compressed (nanofocused)[35] into dimensions dictated by the nanometer-sized apex. Light that is scattered from the apex region is collected in transmission geometry, after passing through the gold-coated glass slide (Figure 1c).
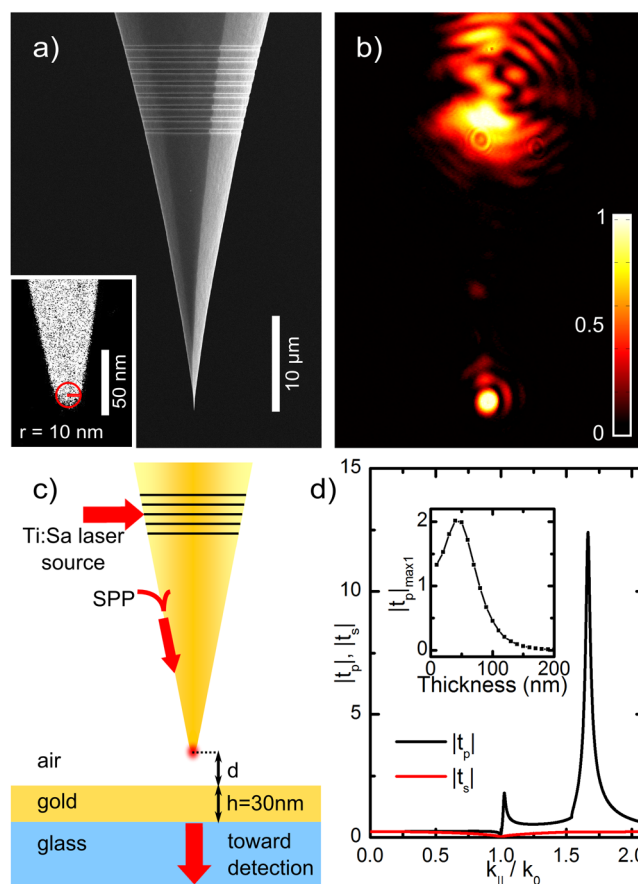

Figure 1. (a) Representative single-crystalline gold taper obtained from an electrochemical etching process. The SEM image shows a smooth surface and an opening angle of around 20°. The apex radius is estimated to be 10 nm. (b) Upon illumination of the grating coupler (upper region), SPPs propagate to the apex (lower region), where light is emitted into the far-field. (c) Sketch of the experimental configuration. A nanofocusing SNOM taper is approached to a $h = 30$ nm thick gold film on a glass substrate. Signals are detected in transmission. (d) Magnitude of the electric field transmission coefficient $|t|$ (obtained from transfer matrix calculations[33]) for the 30 nm gold film depicted in (c) without the taper for s- and p-polarized plane waves as a function of in-plane wavenumber. For p-polarized light, the two resonances reflect the two film SPPs concentrated at the air−gold (in-plane wavevector $k_\parallel \approx 1.03k_0$) and gold−glass interface ($k_\parallel \approx 1.67k_0$), respectively. The inset shows the peak transmission amplitude at the air−gold SPP resonance as a function of film thickness.

As a sample we use a 30 nm thick gold film sputtered onto a BK7 glass coverslip of refractive index $n_{glass} = 1.51$, as indicated in Figure 1c. The gold film can support two distinct film SPPs, whose in-plane wavevector components are $k_\parallel \approx 1.03k_0$ and $k_\parallel \approx 1.67k_0$, with $k_0 = 2\pi/\lambda_0$ being the vacuum wavenumber of the excitation radiation. These SPPs exhibit enhanced field strength at the air−gold interface and the gold−glass interface, respectively. In Figure 1d we show the electric field transmission coefficient $|t|$ for s- and p-polarized plane waves with wavevector $k_\parallel$, passing from the air to the glass side of the film. The values are obtained from a transfer matrix calculation.[33] Evidently, evanescent ($k_\parallel > k_0$), p-polarized field components are strongly enhanced with sharply pronounced maxima at the in-plane wavenumbers of the two film SPP modes. In contrast, s-polarized plane waves cannot couple to

any film SPPs and their transmission amplitude stays below 1.0 for all in-plane wavevectors. The inset of Figure 1d shows that the maximum transmission amplitude for p-polarized radiation exciting the film SPP on the air side occurs for a thickness of the gold of 40 nm. To select the film thickness in our experiments, we have also considered the total power of the detectable leaky evanescent modes ($1 \leq k_{\parallel}/k_0 \leq 1.3$ for an objective with a 1.3 numerical aperture) and the contrast between evanescent ($k_{\parallel} > k_0$) and propagating ($k_{\parallel} < k_0$) signals. The thickness of 30 nm is a trade-off between those considerations. In this way, we optimize the detection of leaky modes, which propagate through glass, away from the gold–glass interface. They are detectable with oil-immersion microscopy as far-field transmission and easily identified in k-space resolved images. The use of an SPP-supporting metal film and leaky mode detection thus provides signal enhancement for the p-polarized evanescent plane wave components, which make up the strong near-field of the $m = 0$ taper mode just beneath the taper apex. Also, the metal film provides the necessary metal–insulator–metal arrangement for gap plasmon formation.

The objective's back-focal plane is projected onto a two-dimensional CCD detector to record the intensity of the spatially Fourier transformed (k-space) fields that are emitted from tip and sample. These images show the intensity of the plane waves with in-plane wavenumber $k_{\parallel}$ and azimuthal angle ϕ, $I(d, k_{\parallel}, \phi)$, that are transmitted through the sample, as a function of tip–sample distance d. They represent Fourier transforms $E(k_x, k_y, z_0; d) = \int\int dx\, dy\, E(x, y, z_0; d)e^{i(k_x x + k_y y)}$ of the electric field $E(x, y, z; d)$ in the plane of the gold–glass interface at $z = z_0$. Here, $(k_x, k_y) = k_{\parallel}(\cos \phi, \sin \phi)$ is the in-plane wavevector. The field at the gold–glass interface is related to the fields at the air–gold interface by $E(k_{\parallel}, \phi, z_0; d) = t_p(k_{\parallel}) \cdot E^{(p)}(k_{\parallel}, \phi, z_0 + h; d) + t_s(k_{\parallel}) \cdot E^{(s)}(k_{\parallel}, \phi, z_0 + h; d)$. Here, t_p and t_s are the transmission coefficients of the gold film for p- and s-polarized light, respectively, obtainable from transfer matrix calculations.[33] The measured intensity is then $I(d, k_{\parallel}, \phi) = |E(k_{\parallel}, \phi, z_0; d)|^2$. The measurements thus give information on the fields that are transmitted through the gold film. Typical images are shown in Figure 2a–c for tip–sample spacings $d = 100$, 10, and 3 nm, respectively. Different signal contributions are readily separated by the magnitude of their in-plane wavevector components $k_{\parallel}$. The inner dashed red circle marks $k_{\parallel} = k_0$. The far-field observable leaky mode contributions extend in principle to the wavenumber in glass, $k_{\parallel} = n_{\text{glass}}k_0 = 1.51k_0$. However, the range accessible with the microscope objective used in our experiments is restricted by its finite numerical aperture of NA = 1.3, marked by the outer dashed red circle in Figure 2a–c.

The intense and rather unstructured signal inside the inner dashed red circle hardly changes with tip–sample distance. This is due to propagating radiation scattered off the grating coupler and taper modes of higher order ($m \neq 0$). As the latter propagate down from the grating along the taper shaft, they are converted into unbound modes at distances of several hundreds of nanometers from the apex. Instead, we focus on signal components outside the inner red circle, with $k_{\parallel} > k_0$, which are related to near-fields in the gap between sample and taper. We will show later that these mainly stem from the $m = 0$ mode. We extract the relevant data for our further discussion exclusively from the recorded intensities between the two red circles.
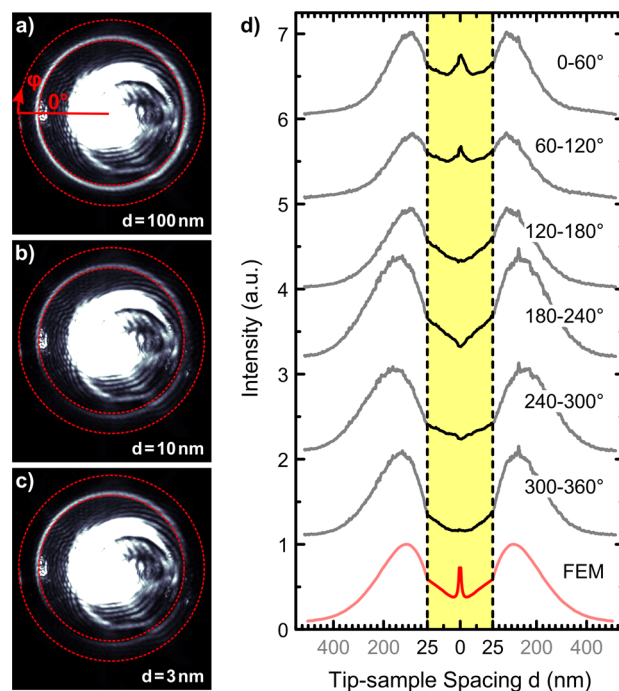

Figure 2. (a–c) Optical k-space images representing the two-dimensional spatial Fourier transform of the radiation emitted from the tip with tip–sample spacings of (a) 100 nm, (b) 10 nm, and (c) 3 nm. The inner dashed red circle marks in-plane k-vectors $k_{\parallel} = k_0 = 2\pi/\lambda_0$ and thus draws the line between far- and near-field contributions. The outer dashed red circle represents the limit imposed by the finite numerical aperture of the microscope objective used (NA = 1.3). Panel (d) shows the integrated signal for $k_0 < k_{\parallel} < 1.3k_0$ in different annular segments (from 0° to 360° in 60° intervals) as a function of tip–sample spacing d. An equivalent signal extracted from a finite element method (FEM) simulation is displayed as a red curve. The left part of the curves represents data acquired during approach; the right part, during retraction of the taper. For clarity, all curves are vertically displaced and a global scaling factor has been applied for comparison to the FEM data. Note that for tip–sample spacings $d < 25$ nm the horizontal axis is stretched by a factor of 5 (yellow-shaded region).

When approaching the gold film to the tip, a ring-shaped pattern appears in the range $k_0 < k_{\parallel} < 1.3k_0$ with maximum brightness at distances of around 100 nm (Figure 2a). The distance dependence of the intensity averaged over an annular segment

$$I_{\text{av}}(d, \phi_1, \phi_2) = \frac{2\pi}{|\phi_2 - \phi_1|} \int_{\phi_1}^{\phi_2} \int_{k_0}^{1.3k_0} d\phi\, dk_{\parallel}\, k_{\parallel} I(d, k_{\parallel}, \phi) \tag{1}$$

is shown in Figure 2d for six different annular segments [ϕ_1, ϕ_2]. The data are normalized to the maximum of the curve averaged over all angles, i.e., $I_{\text{norm}}(d, \phi_1, \phi_2) = I_{\text{av}}(d, \phi_1, \phi_2)/I_{\text{av}}(d_{\text{max}}, 0, 2\pi)$, where d_{max} maximizes $I_{\text{av}}(d, 0, 2\pi)$. In all segments we observe a qualitatively similar dependence of the normalized intensity I_{norm} for large distances ($d > 25$ nm). From $d = 500$ nm to ~200 nm the recorded intensity increases exponentially with decay lengths of $L_D = 100 \pm 30$ nm, depending somewhat on the azimuthal direction. For distances below a single broad maximum at $d \approx 120 \pm 30$ nm, we observe an exponential decrease with nearly the same decay length. For very short distances ($d < 25$ nm, shaded yellow in Figure 2d), the approach curves behave differently in the six annular segments. In particular, we observe a very short-ranged increase

in intensity with a decay length $L_D \approx 5$ nm in the annular interval from 0° to 120°.

We also measure polarization-resolved k-space images for an intermediate tip−sample spacing of 120 nm. As shown in Figure 3, we observe two opposing crescent-moon-shaped lobes
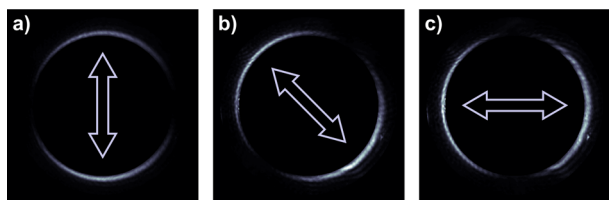

Figure 3. (a−c) Polarization-resolved k-space images for a tip−sample spacing of 120 nm. The polarizer was oriented at 0°, 45°, and 90°, respectively, as indicated by the blue arrows. For clarity, data outside $k_0 < k_\parallel < 1.3k_0$ are masked.

for three different orientations of the polarizer placed in front of the CCD detector. For each polarizer orientation the positions of maximum intensity coincide with the transmission axis. In addition, we measured that circularly polarized contributions (not shown) amount to just 4 ± 3% of the total intensity and can therefore be neglected in good approximation. Hence, this set of polarimetric data allows us to conclude that the recorded fields are indeed radially polarized, which indicates that our k-space imaging scheme is indeed sensitive to the $m = 0$ mode only.

To investigate the origin of the above observations, we perform numerical FEM simulations of the full vectorial electromagnetic fields on a model system. We model the taper as a cylindrical cone with a cone opening angle of 25°,

capped smoothly with a hemispherical apex of 10 nm radius. The sample is approximated as a perfectly smooth two-layer system composed of a 30 nm thick gold film and a glass half-space. The frequency for this monochromatic simulation is set to the center frequency of the laser in the experiment (for further details see the Methods section).[36] As excitation we use only the analytic $m = 0$ mode field of an infinitely long gold cylinder with a radius corresponding to the local radius of the cone at the input boundary.

The simulations are evaluated in a way analogous to the experimental procedure. First, we extract the E-field distribution in a constant-z plane (perpendicular to the taper axis), which is 1 nm below the gold/glass interface. Second, we analyze these fields in terms of an angular spectrum representation via a Hankel transform. The resulting patterns are fully equivalent to the data in Figure 2a−c, and it is hence straightforward to integrate over the relevant annular region characterized by $k_0 < k_\parallel < 1.3k_0$. The result is shown as the red curve at the bottom of Figure 2d. For tip−sample spacings $d > 25$ nm we find excellent agreement with the experiment: The exponential increase in intensity with a decay length of $L_D = 113$ nm in the distance interval $d = 500$ to 220 nm, the maximum intensity at 110 nm, and the exponential decay for tip−sample distances below that compare very well with the behavior observed in experiment. The very sharp increase for distances below the minimum around 5 nm visible in the experimental data for 0−120° is also nicely reproduced.

■ DISCUSSION

The overall convincing agreement between the respective approach curves displayed in Figure 2d establishes a direct connection between our experimental results and the FEM
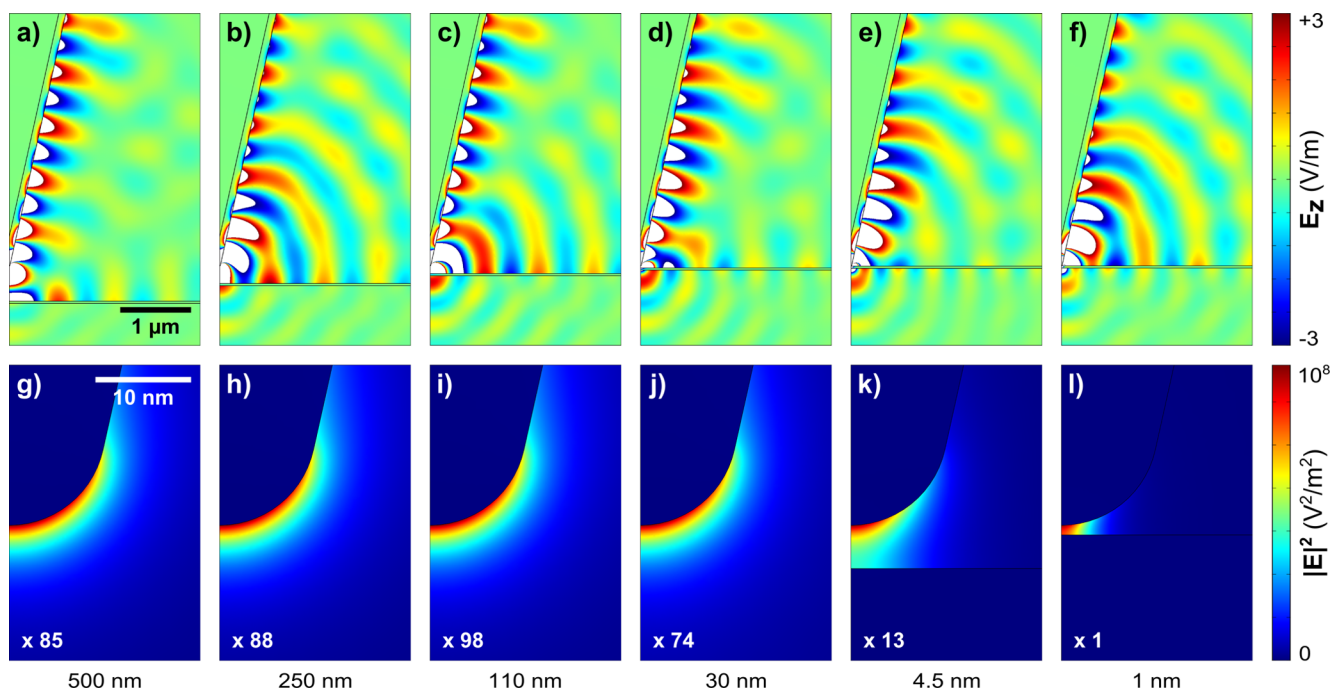

Figure 4. FEM calculations of the field distribution around a metallic cone pointing downward, smoothly capped with a hemispherical apex of radius 10 nm. The rotationally symmetric structure was excited by a radially polarized $m = 0$ cylinder mode at the top of the simulated volume. The tip is placed above a 30 nm thick gold film on top of a glass substrate. The decreasing tip−sample spacing is indicated below the panels. Panels (a)−(f) show the axial field component E_z (white color indicates saturation), while panels (g)−(l) show a detailed view of the apex region for the intensity $|E|^2$. Note that panels (a)−(f) and panels (g)−(l) share the same linear color scales, shown to the right of the panel sets, respectively. Numbers in the lower left corners of panels (g)−(l) indicate multiplying factors that were applied to the data for clarity.

simulations. Most importantly, both experiment and simulation show a distinct enhancement in light scattering intensity for very short tip–sample distances of a few nanometers only. On the basis of this convincing agreement, we argue that this enhancement is a signature of localized plasmon modes in the gap between taper apex and sample.

In experiment, we study the intensity of the light that is scattered from the taper apex and transmitted through the gold film as a function of tip–sample distance. Frequently, such far-field signals from apertureless SNOMs are discussed in the framework of point dipole models,[37,38] and the immediate question arises of whether the physics behind the main features of our approach curves might be captured already by such a comparatively simple model. We assess the applicability of point dipole models in an extended discussion available as Supporting Information and summarize our findings here.

The dipole model predicts an exponential increase in transmitted intensity with a decay length given by the relevant perpendicular k-vector in air $k_\perp(k_\parallel)$ and a short-ranged increase in the near-field regime. As such, neither quasi-static nor fully retarded point dipole models can faithfully account for the approach curves. In particular, they cannot reproduce the maximum near the 110 nm tip–sample distance. Further discrepancies arise in the exponential decay at larger distances between the experimental and FEM data on the one side and the point dipole data on the other. This makes it necessary to also consider the influence of the taper shaft on the light scattering.[39] Whereas the adiabatically nanofocused radiation is emitted from a highly localized region at the very apex of the taper, the reflections from the sample surface interact with the whole taper body. The substantially larger shaft adds contributions to the tip–sample interaction that are not captured by simple point dipole models, leading to qualitatively different behavior.

To take those effects into account and in particular to analyze the steep increase in scattering intensity for tip–sample distances of a few nanometers, we discuss real-space electric field distributions calculated for various tip–sample distances.

We first discuss the coupling between the nanofocused light at the apex and SPP modes of the gold film. For this, we show in Figure 4a–f instantaneous distributions of the calculated field component E_z parallel to the taper axis for selected tip–sample distances. The linear color scale is limited to small field strengths to emphasize the coupling to SPPs. In the white regions, the field amplitudes are up to 3 orders of magnitude higher. The images reveal that SPP waves propagate along the taper surface as a bound mode. Nanofocusing spatially confines the SPP fields and results in strong field enhancement of the field strength near the apex. Furthermore, SPP fields are clearly excited at both interfaces of the gold film. The field patterns both in the apex region and on the film change substantially upon approaching the sample.

For 500 nm tip–sample distance, the fields near the apex scatter predominantly into fields on the air side of the gold layer, including both propagating ($k_\parallel < k_0$) and evanescent ($k_\parallel > k_0$) contributions. For tip–sample distances smaller than 100 nm, fields with a higher spatial frequency of $k_\parallel \approx 1.67k_0$ emerge at the gold–glass interface, corresponding to the excitation of the glass-side film SPP, whose decay length on the intensity level is ~48 nm on the air side. These fields are experimentally not directly observable, as they belong to bound modes of the gold film and decay evanescently in the normal direction. Concurrently with the onset of increasingly stronger excitation

of the $k_\parallel \approx 1.67k_0$ gold film SPP, the power in the observable range of $k_\parallel < 1.3k_0$ appears reduced for distances shorter than $d \approx 110$ nm. That is, a local maximum in the approach curves appears. This observation cannot be understood within any of the point-dipole model variants discussed in the Supporting Information. Rather it points to a more complicated interaction of the sample with the whole taper shaft, as its body penetrates increasingly the evanescent tail of the $k_\parallel \approx 1.03k_0$ air-side gold film SPP, which has a decay length of ~258 nm on the intensity level. As is evident from Figure 2d, the FEM simulations can nicely reproduce the experimental approach curves for tip–sample distances of more than 10 nm and in particular the maximum in scattering intensity at around 110 nm. This suggests that multiple scattering of light that is emitted from the apex region reflected from the sample surface and then back-reflected from the taper shaft contributes significantly to those approach curves.

We now focus on the formation of localized gap plasmon modes. For this, panels (g)–(l) display the patterns of the intensity $|E|^2$ near the apex as close-ups. In this region we find an extreme enhancement in maximum local intensity, which becomes even more pronounced as the tip–sample distance decreases below 100 nm. The corresponding field strengths reach levels that are more than 3 orders of magnitude larger than the maximum of the color scale used for panels (a)–(f). For distances $d > 30$ nm (panels g–i) we find the pattern typical of apex modes,[36,40] which is nearly independent of tip–sample distance. For much smaller distances, however, a drastic transition is observed (panels k, l). The mode field that is forming in the gap between apex and sample surface changes markedly. The mode field appears increasingly confined in both the vertical and lateral dimension. Notably, the maximum intensity increases by another 2 orders of magnitude between panels (i) and (l). Concurrently, the observable far-field intensity increases over the last few nanometers of tip–sample distance. The rather constant field pattern at $d > 30$ nm indicates that the coupling between tip and gold film remains weak and the observed behavior may be described in the framework of perturbation theory. The perturbation description breaks down below 30 nm. The optical interaction of tip and sample cannot be described as a series of multiple reflections anymore. Both the tip apex mode and the surface plasmon modes cease to exist independently, and a new hybrid mode forms, the so-called gap mode.

The concept of gap modes has been invoked previously, for instance, in the context of light emission from small electron tunneling junctions and tip-enhanced Raman spectroscopy.[25–32,41–47] Early theoretical studies usually considered spherical tip models, often in a quasi-static approximation. In contrast to the point-dipole models, however, they use full multipole expansions of the spherical tip to satisfy the boundary conditions also on its surface. As the tip approaches the sample, the distance between the two surfaces goes to zero, in contrast to the distance of the point dipole, which is at minimum the radius of the sphere. This crucial distinction largely explains why the point-dipole model remains weakly coupled and fails to properly account for our findings. Indeed, entering the strong coupling regime may also be thought of as coupling of dipolar excitations to higher order multipolar excitations of the tip. The more realistic FEM simulations presented here allow us to test the well-known estimate for the field confinement as proportional to the geometric mean of tip–sample distance and the effective radius of curvature of the apex. From intensity maps

such as those displayed in Figure 4, we derive a quantitative description of the lateral mode confinement in the gap, just below the apex. Figure 5 shows the lateral full width at half-
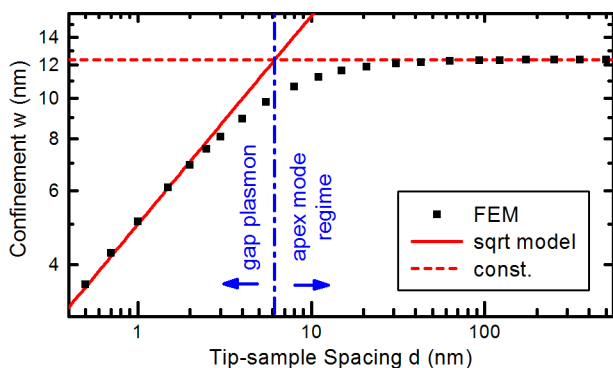

Figure 5. Lateral confinement w of the intensity $|E|^2$ obtained as full width at half-maximum from cross-sections through the simulated field patterns 0.2 nm away from the apex for different tip−sample spacings d. A square root model[32] for the gap plasmon extent, $w = A\sqrt{Rd}$, was fitted to the data with tip−sample spacing $d \leq 2$ nm, shown as the solid red line. For $R = 10$ nm an optimum value of $A = 1.57$ is found. The red dashed line represents a constant fit to the data with tip−sample spacing $d \geq 100$ nm.

maximum (w) as a function of tip−sample distance, as evaluated from FEM results (black squares) and the asymptotic trends for large and vanishing distances (red dashed and solid lines, respectively). For distances $d \gg 6$ nm the intensity profile exhibits a width of $w \approx 2\sqrt{\sqrt{2} - 1}\, R$. This is the value expected for the apex mode of isolated conical tapers, whose field pattern is nearly Lorentzian.[48] For distances $d \ll 6$ nm, the confinement asymptotically follows

$$w \approx 1.57\sqrt{Rd} \tag{2}$$

which confirms earlier reports.[32] For a tip−sample spacing of $d = 0.5$ nm, which is well above the reasonable lower limit of 0.3 nm for classical electrodynamics to hold,[26] the lateral extent of the gap plasmon intensity profile has decreased by a factor of almost 4 to $w \approx 3.5$ nm.

Evidently, this gap mode formation is revealed in the experimental approach curves only for azimuthal angles of 0−120° (Figure 2d). This is in contrast to the rotational symmetry of the FEM simulations. We attribute this difference to faceting and other deviations from perfect rotational symmetry of the single-crystalline taper body. Since the spatial extent of the optical near-field is so short, even minor deviations from perfect rotational symmetry will result in anisotropic scattering patterns. Such deviations are clearly unavoidable with our fabrication method. In particular, a taper structure whose apex appears locally as a slightly tilted cone gives rise to preferred emission of radiation into certain azimuthal directions. In the Supporting Information section we discuss a numerical study of such a tilted configuration that demonstrates the possibly strong anisotropic effect of such a tilt (Figure S3). This indicates that the angular distribution of the experimental signal strongly depends on the shape and alignment of the taper. It should be noted that the underlying fundamental principle of adiabatic nanofocusing applies, nevertheless. Adiabaticity also applies to changes to the cross sectional shape other than circular concentration. Our results show that, experimentally, angle-resolved k-space imaging is a powerful method to reveal those anisotropies.

The FEM calculations provide clear evidence that the increase in scattering intensity seen in the k-space images for distances of less than 10 nm is a direct signature of gap plasmons formed in the junction between taper apex and gold surface. The convincing agreement of amplitude and range of the scattering enhancement in experiment and the FEM model suggests that this gap mode formation also governs the experimental approach curves for small distance. In principle, one may argue that such a localization signature may also arise from the coupling of the apex mode to localized SPPs of the gold film with finite surface roughness. To rule out this alternative interpretation, we have recorded spatially resolved approach curves on both a planar polycrystalline gold film and a slit grating milled into a 30 nm thick gold film (Figure 6). The measurements are performed in a reflection geometry, collecting light from the apex region without angular resolution. Rather than k-space-resolved data, they present approach curves over linearly spaced positions on the sample surface.
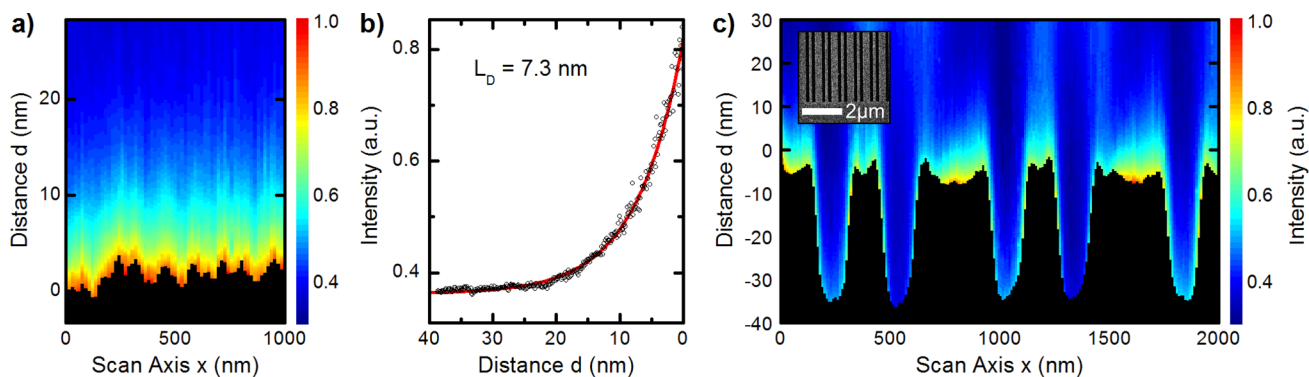

Figure 6. Nanofocusing light backscattering images (see Methods sections for details) from the apex of a gold taper as a function of distance d between the tip apex and the sample and lateral sample position x. The light scattering intensity collected on the tip side of the sample is plotted on a linear scale. The data in panel (a) were recorded on a nominally flat, polycrystalline gold film of 30 nm thickness. Panel (b) shows a single signal trace along d extracted from panel (a) at $x = 440$ nm. The red curve is an exponential fit to the data with a decay length of $L_D = 7.3$ nm. Panel (c) shows a data set recorded under equivalent conditions to the one in panel (a), but on a slit grating milled into a 30 nm thick polycrystalline gold film deposited on a glass surface. A scanning electron micrograph top view image of the grating is shown in the inset of (c).

In panel (a) we show a backscattering image of the planar, 30 nm thick gold film. From the topographical information in panel (a), we deduce typical height variations on the order of 2 nm over lateral distances of a few tens of nanometers. The light scattering image reveals a pronounced, more than 3-fold increase in near-field scattering intensity when approaching tip and sample surface to distances of less than 10 nm. Panel (b) shows a single approach curve extracted from panel (a) at the lateral position x = 440 nm. We fit a monoexponential decay model to this curve. This results in an intensity decay length of only L_D = 7.3 nm for the near-field contrast and matches nicely with that seen in Figure 2d. This is the signature of the coupling of the localized near-field at the taper apex to local optical near-fields at the sample surface. For the planar film, lateral variations in scattering intensity are very small. Hence these approach curves show no evidence of lateral confinement reflecting SPP localization due to surface roughness.

Panel (c) displays approach curves over the slit grating as an example for a spatially inhomogeneous sample. Here, the scattered intensity also shows a 3-fold enhancement when approaching tip and sample, but enhancement varies distinctly with lateral position. Laterally, the field intensity is localized on a 100 nm scale on the ridges. In the grooves the bare glass substrate is exposed. There, we find comparatively low enhancement in scattered intensity. The overall pattern reveals the formation of standing SPP modes at the metal/air interface of the grating, with field maxima in the center of the wide stripes.[49]

Evidently, the images show no signatures of random field fluctuations on shorter length scales. We take this as evidence that plasmon localization due to the finite roughness of the gold film is negligible in our experiments. This supports our conclusion that the sharp increase in scattering intensity for few nanometer distances in Figure 2d indeed reflects optical gap mode formation.

CONCLUSION

We have presented k-vector-resolved measurements on the distance-dependent near-field coupling between a nanofocusing conical gold taper and a metallic substrate. The experiments show a steep increase in scattering intensity within the last 5 nm in certain scattering directions. Detailed FEM simulations could reproduce all prominent experimental features and reveal unequivocally that the rapid increase in far-field-detectable scattering intensity at nearly vanishing tip−sample distances is a clear signature of the formation of strongly coupled gap modes, confined between the taper apex and the sample surface.

The approach for generating gap plasmons presented here distinguishes itself from conventional apertureless scattering-type SNOM through the combination with adiabatic nanofocusing. Conventional excitation geometries rely on placing the gap volume inside the much larger far-field focus, and the unwanted scattering from an extended sample region usually requries some form of modulation/demodulation scheme. This is not necessary in our scheme. Our results clearly demonstrate that gap plasmon formation with adiabatic nanofocusing on single-crystalline gold tapers is a viable and intriguing alternative that provides direct access to the near-field generated signal on a much reduced background. This relative background suppression is further improved through the combination with the near-field contrast, enhancing transmission through a semitransparent metal film and discrimination of evanescent field components in k-space.

Our results indicate two particularly interesting aspects of this approach. First, it allows confining light at the very apex of the taper to dimensions that are not limited by its apex diameter. For realistic taper diameters of 10−20 nm, we estimate a spatial resolution of 2.5−5 nm. The feasibility of lateral resolution below the apex radius using gap mode formation has been demonstrated in previous studies involving inelastic optical signals, such as photoluminescence or Raman scattering.[50−52] The scheme presented here holds the promise of extending the applicability of gap-plasmon-enhanced near-field optical microscopy also to the elastic channel. Ultimately, tapers with $R \leq 5$ nm lie within the accessible tail of the distribution achieved in our current taper fabrication scheme (see Methods section). That is, a lateral optical resolution of better than 2.5 nm appears feasible even within the classical electrodynamics regime. For even smaller distances, entering the quantum tunneling regime, the intriguing question arises whether optically induced quantum tunneling may lead to atomic resolution as is achieved in electronically driven scanning tunneling microscopy.

Second, the local field intensity of a gap plasmon can exceed that of a bare apex mode by at least 2 orders of magnitude. Correspondingly more photons are available per unit time and area for optical excitation, which benefits especially nonlinear processes such as Raman scattering.[31,52−55] Even for linear processes such as elastic scattering or molecular absorption the corresponding interaction cross-sections (up to $\sim 10^{-14}$ cm^2 [24]) are close to the achievable intensity cross-sections of gap plasmons (4.8×10^{-14} cm^2 for R = 5 nm and d = 0.5 nm). Using adiabatically excited gap plasmons thus opens the door to nearly background-free, high-speed, and hyperspectral nanoscopic spectroscopy of individual emitters with high sensitivity.

METHODS

SNOM Tapers. Nanofocusing SNOM tapers were obtained from a procedure described earlier.[15] Au wires (125 μm, Advent Research) were thermally annealed followed by ac etching in hydrochloric acid against a Pt counter electrode (Advent Research). After characterization by scanning electron microscopy the grating coupler was produced by focused Ga ion beam milling (FEI Helios 500).

Sample Fabrication. Thirty nanometer thick Au films were produced by electron-beam evaporation (HHV FL400) on standard microscopy coverslips (BK7, Menzel-Gläser) after cleaning with chromic-sulfuric acid and distilled water.[56] The grating shown in Figure 6c was milled into such a gold film by focused Ga$^+$ ion milling. The grating period is 800 nm, with two 150 nm wide and 30 nm deep grooves per period, separated by 150 and 350 nm wide gold ridges.

Distance Control. The taper is carefully aligned with its axis perpendicular to the sample surface. The distance between both is controlled with a tuning fork based atomic force microscope. The taper oscillates normal to the sample surface in the noncontact regime, avoiding any snap-in events. The free probe oscillation amplitude at large distances is below 1 nm. In order to avoid mechanical damage to the tip apex during measurements, tip−sample approaches are stopped when mechanical damping of the tuning fork leads to a decrease in tapping amplitude by more than 15% of the absolute signal. The absolute tip−sample distance is calibrated in independent tests with similar tips, in which they are brought into physical contact with the sample in a controlled manner (see also

Supporting Information). Typically, the stopping condition in the experiments reported here corresponds to an average distance of 1.8 nm with an oscillation amplitude of 0.8 nm.

Signal Collection *k*-Space. The light emitted from the apex is transmitted through the gold film and glass substrate and collected with a high numerical aperture microscope objective (NA = 1.3). We always align our imaging system such that the tip apex is in the center of the focal volume when the sample is in contact. During an approach/retract cycle tip and microscope objective remain spatially fixed, while the sample moves up to 500 nm away from the tip. This motion changes the optical path distance to the detector by $(n_{oil} - n_{air}) \times 500$ nm ≈ 250 nm, which is well within the depth of field of the imaging system of about 770 nm. That is, the tip apex remains within the focus volume at all times, and this slow and monotonous change to the imaging system does not significantly impact the signal traces obtained in the approach curves. The *k*-space setup is a modified version of the one described earlier.[34] It utilizes two lenses and an iris arranged in 4-f geometry between the objective's back-focal plane and the CCD detector to spatially filter a region of about 10 μm in diameter, centered on the apex. For polarization-dependent measurements a polarizer (Codixx) was inserted in front of the CCD camera.

Signal Collection Backscattering. Far-field light is coupled onto a grating coupler on the taper shaft and nanofocused to the apex. The light scattered from the apex region is collected on the tip side of the sample with a microscope objective with a numerical aperture of 0.35. The sample is repeatedly approached along the vertical tip−sample axis at linearly spaced sample positions. This results in two-dimensional images showing the position-dependent signal in a plane normal to the sample surface.

FEM Simulations. The simulation was carried out using the finite element method (COMSOL Multiphysics) in 2D axisymmetry mode with full vectorial field components. The size of the simulation domain containing gold taper and gold-coated glass substrate was 3.5 μm (horizontal) by 5.5 μm (vertical), including 800 nm wide perfectly matched layers. The apex radius and cone opening angle of the taper were set to 10 nm and 25°, respectively. The thickness of the film was set to 30 nm. The relative permittivity for gold, $\varepsilon_{Au} = -24.747 + 1.8834i$ at $\lambda_0 = 800$ nm, was taken from a fit to literature data.[57] The value for glass was set to $\varepsilon_{glass} = 2.28$ (BK7). By using port boundary conditions at the upper end of the simulation domain, we can excite our precise taper eigenmode and also absorb waves that propagate to this boundary. To keep the excitation power and also modal shape the same for all tip−sample spacings *d*, the position of the taper was fixed while changing the position of the gold-coated glass substrate. The maximum mesh size in air and glass was set to $\lambda_{air}/20$ and $\lambda_{glass}/20$, respectively, except for the vicinity of the apex, where the maximum mesh size was set to 0.1 nm. All calculations were verified by convergence tests. For comparison with the experimental data, the field distribution was extracted in a plane inside the glass half-space and 1 nm away from the gold−glass interface and subsequently converted to 2D *k*-space data using a Hankel transform.

ASSOCIATED CONTENT

Ⓢ Supporting Information

The Supporting Information is available free of charge on the ACS Publications website at DOI: 10.1021/acsphotonics.5b00438.

> Assessment of the applicability of point dipole models for the description of the experimental findings, calibration data of tip−sample distance, and numerical study of the influence of relative tilt between tip and sample (PDF)

AUTHOR INFORMATION

Corresponding Author

*E-mail: simon.f.becker@uni-oldenburg.de.

Author Contributions

S.F.B. and M.E. did the experiments. K.W.Y. performed the FEM simulations. The manuscript was written through contributions of all authors. All authors have given approval to the final version of the manuscript.

Notes

The authors declare no competing financial interest.

ACKNOWLEDGMENTS

REFERENCES

(1) Bottomley, L. A. Scanning probe microscopy. *Anal. Chem.* **1998**, 70, 425−475.

(2) Berweger, S.; Atkin, J. M.; Olmon, R. L.; Raschke, M. B. Light on the Tip of a Needle: Plasmonic Nanofocusing for Spectroscopy on the Nanoscale. *J. Phys. Chem. Lett.* **2012**, 3, 945−952.

(3) Pettinger, B.; Schambach, P.; Villagomez, C. J.; Scott, N. Tip-Enhanced Raman Spectroscopy: Near-Fields Acting on a Few Molecules. *Annu. Rev. Phys. Chem.* **2012**, 63, 379−399.

(4) Xu, X. J. G.; Rang, M.; Craig, I. M.; Raschke, M. B. Pushing the Sample-Size Limit of Infrared Vibrational Nanospectroscopy: From Monolayer toward Single Molecule Sensitivity. *J. Phys. Chem. Lett.* **2012**, 3, 1836−1841.

(5) Wagner, M.; McLeod, A. S.; Maddox, S. J.; Fei, Z.; Liu, M. K.; Averitt, R. D.; Fogler, M. M.; Bank, S. R.; Keilmann, F.; Basov, D. N. Ultrafast Dynamics of Surface Plasmons in InAs by Time-Resolved Infrared Nanospectroscopy. *Nano Lett.* **2014**, 14, 4529−4534.

(6) Wagner, M.; Fei, Z.; McLeod, A. S.; Rodin, A. S.; Bao, W. Z.; Iwinski, E. G.; Zhao, Z.; Goldflam, M.; Liu, M. K.; Dominguez, G.; Thiemens, M.; Fogler, M. M.; Neto, A. H. C.; Lau, C. N.; Amarie, S.; Keilmann, F.; Basov, D. N. Ultrafast and Nanoscale Plasmonic Phenomena in Exfoliated Graphene Revealed by Infrared Pump-Probe Nanoscopy. *Nano Lett.* **2014**, 14, 894−900.

(7) Scholes, G. D.; Fleming, G. R.; Olaya-Castro, A.; van Grondelle, R. Lessons from nature about solar light harvesting. *Nat. Chem.* **2011**, 3, 763−774.

(8) Falke, S. M.; Rozzi, C. A.; Brida, D.; Maiuri, M.; Amato, M.; Sommer, E.; De Sio, A.; Rubio, A.; Cerullo, G.; Molinari, E.; Lienau, C. Coherent ultrafast charge transfer in an organic photovoltaic blend. *Science* **2014**, 344, 1001−1005.

(9) van Schrojenstein Lantman, E. M.; Deckert-Gaudig, T.; Mank, A. J. G.; Deckert, V.; Weckhuysen, B. M. Catalytic processes monitored at

the nanoscale with tip-enhanced Raman spectroscopy. *Nat. Nanotechnol.* **2012**, *7*, 583−586.

(10) Wu, K. F.; Zhu, H. M.; Liu, Z.; Rodriguez-Cordoba, W.; Lian, T. Q. Ultrafast Charge Separation and Long-Lived Charge Separated State in Photocatalytic CdS-Pt Nanorod Heterostructures. *J. Am. Chem. Soc.* **2012**, *134*, 10337−10340.

(11) Babadjanyan, A. J.; Margaryan, N. L.; Nerkararyan, K. V. Superfocusing of surface polaritons in the conical structure. *J. Appl. Phys.* **2000**, *87*, 3785−3788.

(12) Stockman, M. I. Nanofocusing of Optical Energy in Tapered Plasmonic Waveguides (vol 93, 137404, 2004). *Phys. Rev. Lett.* **2011**, *106*, 019901.

(13) Stockman, M. I. Nanofocusing of optical energy in tapered plasmonic waveguides. *Phys. Rev. Lett.* **2004**, *93*, 137404.

(14) Zaccaria, R. P.; Alabastri, A.; De Angelis, F.; Das, G.; Liberale, C.; Toma, A.; Giugni, A.; Razzari, L.; Malerba, M.; Sun, H. B.; Di Fabrizio, E. Fully analytical description of adiabatic compression in dissipative polaritonic structures. *Phys. Rev. B: Condens. Matter Mater. Phys.* **2012**, *86*, 035410.

(15) Schmidt, S.; Piglosiewicz, B.; Sadiq, D.; Shirdel, J.; Lee, J. S.; Vasa, P.; Park, N.; Kim, D. S.; Lienau, C. Adiabatic Nanofocusing on Ultrasmooth Single-Crystalline Gold Tapers Creates a 10-nm-Sized Light Source with Few-Cycle Time Resolution. *ACS Nano* **2012**, *6*, 6040−6048.

(16) Kravtsov, V.; Atkin, J. M.; Raschke, M. B. Group delay and dispersion in adiabatic plasmonic nanofocusing. *Opt. Lett.* **2013**, *38*, 1322−1324.

(17) Neacsu, C. C.; Berweger, S.; Olmon, R. L.; Saraf, L. V.; Ropers, C.; Raschke, M. B. Near-Field Localization in Plasmonic Superfocusing: A Nanoemitter on a Tip. *Nano Lett.* **2010**, *10*, 592−596.

(18) Gerton, J. M.; Wade, L. A.; Lessard, G. A.; Ma, Z.; Quake, S. R. Tip-enhanced fluorescence microscopy at 10 nm resolution. *Phys. Rev. Lett.* **2004**, *93*, 180801.

(19) Zhang, D.; Heinemeyer, U.; Stanciu, C.; Sackrow, M.; Braun, K.; Hennemann, L. E.; Wang, X.; Scholz, R.; Schreiber, F.; Meixner, A. J. Nanoscale Spectroscopic Imaging of Organic Semiconductor Films by Plasmon-Polariton Coupling. *Phys. Rev. Lett.* **2010**, *104*, 056601.

(20) Hartschuh, A.; Pedrosa, H. N.; Novotny, L.; Krauss, T. D. Simultaneous fluorescence and Raman scattering from single carbon nanotubes. *Science* **2003**, *301*, 1354−1356.

(21) Hartschuh, A.; Sanchez, E. J.; Xie, X. S.; Novotny, L. High-resolution near-field Raman microscopy of single-walled carbon nanotubes. *Phys. Rev. Lett.* **2003**, *90*, 095503.

(22) Sadiq, D.; Shirdel, J.; Lee, J. S.; Selishcheva, E.; Park, N.; Lienau, C. Adiabatic Nanofocusing Scattering-Type Optical Nanoscopy of Individual Gold Nanoparticles. *Nano Lett.* **2011**, *11*, 1609−1613.

(23) Zhang, Z.; Ahn, P.; Dong, B. Q.; Balogun, O.; Sun, C. Quantitative Imaging of Rapidly Decaying Evanescent Fields Using Plasmonic Near-Field Scanning Optical Microscopy. *Sci. Rep.* **2013**, *3*, 2803.

(24) Rothman, L. S.; Gordon, I. E.; Babikov, Y.; Barbe, A.; Benner, D. C.; Bernath, P. F.; Birk, M.; Bizzocchi, L.; Boudon, V.; Brown, L. R.; Campargue, A.; Chance, K.; Cohen, E. A.; Coudert, L. H.; Devi, V. M.; Drouin, B. J.; Fayt, A.; Flaud, J. M.; Gamache, R. R.; Harrison, J. J.; Hartmann, J. M.; Hill, C.; Hodges, J. T.; Jacquemart, D.; Jolly, A.; Lamouroux, J.; Le Roy, R. J.; Li, G.; Long, D. A.; Lyulin, O. M.; Mackie, C. J.; Massie, S. T.; Mikhailenko, S.; Muller, H. S. P.; Naumenko, O. V.; Nikitin, A. V.; Orphal, J.; Perevalov, V.; Perrin, A.; Polovtseva, E. R.; Richard, C.; Smith, M. A. H.; Starikova, E.; Sung, K.; Tashkun, S.; Tennyson, J.; Toon, G. C.; Tyuterev, V. G.; Wagner, G. The HITRAN2012 molecular spectroscopic database. *J. Quant. Spectrosc. Radiat. Transfer* **2013**, *130*, 4−50.

(25) Aubry, A.; Lei, D. Y.; Maier, S. A.; Pendry, J. B. Plasmonic Hybridization between Nanowires and a Metallic Surface: A Transformation Optics Approach. *ACS Nano* **2011**, *5*, 3293−3308.

(26) Savage, K. J.; Hawkeye, M. M.; Esteban, R.; Borisov, A. G.; Aizpurua, J.; Baumberg, J. J. Revealing the quantum regime in tunnelling plasmonics. *Nature* **2012**, *491*, 574−577.

(27) Porto, J. A.; Johansson, P.; Apell, S. P.; Lopez-Rios, T. Resonance shift effects in apertureless scanning near-field optical microscopy. *Phys. Rev. B: Condens. Matter Mater. Phys.* **2003**, *67*, 085409.

(28) Lei, D. Y.; Fernandez-Dominguez, A. I.; Sonnefraud, Y.; Appavoo, K.; Haglund, R. F.; Pendry, J. B.; Maier, S. A. Revealing Plasmonic Gap Modes in Particle-on-Film Systems Using Dark-Field Spectroscopy. *ACS Nano* **2012**, *6*, 1380−1386.

(29) Lumdee, C.; Yun, B. F.; Kik, P. G. Gap-Plasmon Enhanced Gold Nanoparticle Photoluminescence. *ACS Photonics* **2014**, *1*, 1224−1230.

(30) Esteban, R.; Vogelgesang, R.; Kern, K. Tip-substrate interaction in optical near-field microscopy. *Phys. Rev. B: Condens. Matter Mater. Phys.* **2007**, *75*, 195410.

(31) Stadler, J.; Oswald, B.; Schmid, T.; Zenobi, R. Characterizing unusual metal substrates for gap-mode tip-enhanced Raman spectroscopy. *J. Raman Spectrosc.* **2013**, *44*, 227−233.

(32) Rendell, R. W.; Scalapino, D. J. Surface-Plasmons Confined by Microstructures on Tunnel-Junctions. *Phys. Rev. B: Condens. Matter Mater. Phys.* **1981**, *24*, 3276−3294.

(33) Klein, M. V.; Furtak, T. E. *Optics*, 2nd ed.; Wiley, 1986.

(34) Esmann, M.; Becker, S. F.; da Cunha, B. B.; Brauer, J. H.; Vogelgesang, R.; Gross, P.; Lienau, C. k-space imaging of the eigenmodes of sharp gold tapers for scanning near-field optical microscopy. *Beilstein J. Nanotechnol.* **2013**, *4*, 603−610.

(35) Ropers, C.; Neacsu, C. C.; Elsaesser, T.; Albrecht, M.; Raschke, M. B.; Lienau, C. Grating-coupling of surface plasmons onto metallic tips: A nanoconfined light source. *Nano Lett.* **2007**, *7*, 2784−2788.

(36) Issa, N. A.; Guckenberger, R. Optical nanofocusing on tapered metallic waveguides. *Plasmonics* **2007**, *2*, 31−37.

(37) Knoll, B.; Keilmann, F. Enhanced dielectric contrast in scattering-type scanning near-field optical microscopy. *Opt. Commun.* **2000**, *182*, 321−328.

(38) Koglin, J.; Fischer, U. C.; Fuchs, H. Material contrast in scanning near-field optical microscopy at 1−10 nm resolution. *Phys. Rev. B: Condens. Matter Mater. Phys.* **1997**, *55*, 7977−7984.

(39) Stebounova, L.; Akhremitchev, B. B.; Walker, G. C. Enhancement of the weak scattered signal in apertureless near-field scanning infrared microscopy. *Rev. Sci. Instrum.* **2003**, *74*, 3670−3674.

(40) Novotny, L.; Bian, R. X.; Xie, X. S. Theory of nanometric optical tweezers. *Phys. Rev. Lett.* **1997**, *79*, 645−648.

(41) Rendell, R. W.; Scalapino, D. J.; Muhlschlegel, B. Role of Local Plasmon Modes in Light-Emission from Small-Particle Tunnel-Junctions. *Phys. Rev. Lett.* **1978**, *41*, 1746−1750.

(42) Aravind, P. K.; Metiu, H. The Effects of the Interaction between Resonances in the Electromagnetic Response of a Sphere-Plane Structure - Applications to Surface Enhanced Spectroscopy. *Surf. Sci.* **1983**, *124*, 506−528.

(43) Malshukov, A. G. Surface-Enhanced Raman-Scattering - the Present Status. *Phys. Rep.* **1990**, *194*, 343−349.

(44) Konopsky, V. N. Operation of scanning plasmon near-field microscope with gold and silver tips in tapping mode: demonstration of subtip resolution. *Opt. Commun.* **2000**, *185*, 83−93.

(45) Gozhenko, V. V.; Grechko, L. G.; Whites, K. W. Electrodynamics of spatial clusters of spheres: Substrate effects. *Phys. Rev. B: Condens. Matter Mater. Phys.* **2003**, *68*, 125422.

(46) Notingher, I.; Elfick, A. Effect of sample and substrate electric properties on the electric field enhancement at the apex of SPM nanotips. *J. Phys. Chem. B* **2005**, *109*, 15699−15706.

(47) Downes, A.; Salter, D.; Elfick, A. Simulations of atomic resolution tip-enhanced optical microscopy. *Opt. Express* **2006**, *14*, 11324−11329.

(48) Esteban, R.; Vogelgesang, R.; Kern, K. Simulation of optical near and far fields of dielectric apertureless scanning probes. *Nanotechnology* **2006**, *17*, 475−482.

(49) Ropers, C.; Park, D. J.; Stibenz, G.; Steinmeyer, G.; Kim, J.; Kim, D. S.; Lienau, C. Femtosecond light transmission and subradiant damping in plasmonic crystals. *Phys. Rev. Lett.* **2005**, *94*, 113901.

(50) Sackrow, M.; Stanciu, C.; Lieb, M. A.; Meixner, A. J. Imaging Nanometre-Sized Hot Spots on Smooth Au Films with High-

Resolution Tip-Enhanced Luminescence and Raman Near-Field Optical Microscopy. *ChemPhysChem* **2008**, *9*, 316−320.

(51) Fleischer, M.; Stanciu, C.; Stade, F.; Stadler, J.; Braun, K.; Heeren, A.; Häffner, M.; Kern, D. P.; Meixner, A. J. Three-dimensional optical antennas: Nanocones in an apertureless scanning near-field microscope. *Appl. Phys. Lett.* **2008**, *93*, 111114.

(52) Zhang, R.; Zhang, Y.; Dong, Z. C.; Jiang, S.; Zhang, C.; Chen, L. G.; Zhang, L.; Liao, Y.; Aizpurua, J.; Luo, Y.; Yang, J. L.; Hou, J. G. Chemical mapping of a single molecule by plasmon-enhanced Raman scattering. *Nature* **2013**, *498*, 82−86.

(53) Schmid, T.; Opilik, L.; Blum, C.; Zenobi, R. Nanoscale Chemical Imaging Using Tip-Enhanced Raman Spectroscopy: A Critical Review. *Angew. Chem., Int. Ed.* **2013**, *52*, 5940−5954.

(54) Schultz, Z. D.; Marr, J. M.; Wang, H. Tip enhanced Raman scattering: plasmonic enhancements for nanoscale chemical analysis. *Nanophotonics* **2014**, *3*, 91−104.

(55) Mauser, N.; Hartschuh, A. Tip-enhanced near-field optical microscopy. *Chem. Soc. Rev.* **2014**, *43*, 1248−1262.

(56) Kollmann, H.; Piao, X.; Esmann, M.; Becker, S. F.; Hou, D. C.; Huynh, C.; Kautschor, L. O.; Bosker, G.; Vieker, H.; Beyer, A.; Golzhauser, A.; Park, N.; Vogelgesang, R.; Silies, M.; Lienau, C. Toward Plasmonics with Nanometer Precision: Nonlinear Optics of Helium-Ion Milled Gold Nanoantennas. *Nano Lett.* **2014**, *14*, 4778−4784.

(57) Johnson, P. B.; Christy, R. W. Optical Constants of Noble Metals. *Phys. Rev. B* **1972**, *6*, 4370−4379.